

60 GHz millimeter-wave indoor propagation path loss models for modified indoor environments

Nidal Qasem, Mohammad Alkhatrah

Department of Communications and Computer Engineering, Al-Ahliyya Amman University, Amman, Jordan

Article Info

Article history:

Received Nov 19, 2023

Revised Feb 5, 2024

Accepted Feb 9, 2024

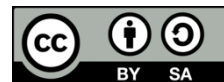
Keywords:

60 GHz band
Frequency selective surface
Indoor wireless
Millimeter wave
Path loss model

ABSTRACT

The 60 GHz band has been selected for short-range communication systems to meet consumers' needs for high data rates. However, this frequency is attenuated by obstacles. This study addresses the limitations of the 60 GHz band by modifying indoor environments with square loop (SL) frequency selective surfaces (FSSs) wallpaper, thereby increasing its utilization. The SL FSS wallpaper response at a 61.5 GHz frequency has been analyzed using both MATLAB and CST Studio Suite software. 'Wireless InSite' is also used to demonstrate enhanced wave propagation in a building modified with SL FSSs wallpaper. The demonstration is applied to multiple input multiple output system to verify the effectiveness of FSSs on such systems' capacity, as well as the effect of the human body on capacity. Simulation results presented here show that modifying a building using SL FSS wallpaper is an attractive scheme for significantly improving the indoor 60 GHz wireless communications band. This paper also presents and compares two large-scale indoor propagation path loss models, the close-in (CI) free space reference distance model and the floating intercept (FI) model. Data obtained from 'Wireless InSite' over distances ranging from 4 to 14.31 m is analyzed. Results show that the CI model provides good estimation and exhibits stable behavior over frequencies and distances, with a solid physical basis and less computational complexity when compared to the FI model.

This is an open access article under the [CC BY-SA](https://creativecommons.org/licenses/by-sa/4.0/) license.



Corresponding Author:

Nidal Qasem

Department of Communications and Computer Engineering, Faculty of Engineering, Al-Ahliyya Amman University

Zip-code (Postal Address): 19328, Amman, Jordan

Email: Ne.qasem@ammanu.edu.jo

1. INTRODUCTION

The 60 GHz band is a perfect choice for achieving the desired goal of obtaining high-speed data rates with a theoretical upper limit of 6.5 gigabit-per-second. It also provides benefits, such as a 10 W maximum transmit power, a high level of frequency reuse, and a high level of savings in operations [1]–[3]. When comparing the 60 GHz band with other unlicensed bands, it can be seen that the 60 GHz band provides much higher data rates. However, it is easily blocked by obstacles, and this places more restrictions on using it. For example, concrete materials, glass, walls, and the human body can cause large signal attenuation on a 60 GHz band. Thus, the 60 GHz communication band is more suitable for indoor and short-range environments in which sufficient reflectors are present [4].

The unlicensed 60 GHz band allocates 9 GHz sub-bands, which varies slightly depending on local regulations. Technical standards divide this band into four 2.16 GHz channels. The 61.5 GHz frequency

which allocates at the second channel has been selected for this study since it is commonly used as an unlicensed frequency in different regions and countries [5].

Indoor channel simulations/measurements are vital to understanding path loss (PL) as a function of distance, and temporal and spatial characteristics, which are crucial in performing system-wide simulations to estimate network system capacities and overall data throughputs. PL models (PLMs) are very important models with which to comprehend and study the attenuation of signal propagation from transmitters (Tx's) to receivers (Rx's) and allow accurate channel models to be designed for network simulations, which, in turn, help in designing communication systems. The most common single-frequency PLMs are close-in (CI) and floating intercept (FI). Both of these models will be studied in this paper [6].

This study focuses on utilization by suggesting an unprecedented technique that can control the propagation of the indoor wireless environment of the 60 GHz band by completely reflecting the entire 60 GHz band, keeping it inside the area of interest. This technique uses square loop (SL) frequency selective services (FSSs) wallpaper in order to provide a more strongly received signal; it does this by increasing the multipath propagation due to the variety of signal paths. In addition, this research provides a comprehensive study of indoor propagation at the 60 GHz band by using different scenarios to generate a large-scale PL model (PLM) for enhancing 5th generation standards at the 60 GHz band. In any case, extensive indoor propagation simulations at the 60 GHz band are needed in order to accurately characterize and model the channel needed to design a capable indoor system at this frequency.

This paper is organized as follows: section 2 explains the equivalent circuit model (ECM) analyzes technique and applies it to the SL FSS wallpaper. As well as it explains large-sale PLMs. Next, section 3 examines the simulation results and discussion. It starts with SL FSS wallpaper, and its transmission and reflection coefficients, using both MATLAB and CST Studio Suite. Then, demonstrates investigations of some selected scenarios using 'Wireless InSite', these scenarios have been tested based on multiple input multiple output (MIMO) case. MIMO case is presented and performed both with/without SL FSS wallpaper to investigate SL FSS wallpaper's effect on the received signal power, both in the presence and absence of human bodies. In addition, it presents PLMs results. Finally, section 4 concludes this paper.

2. SYSTEM MODEL

2.1. SL FSS wallpaper

FSSs are planar periodic structures that can be used as a filter for a specific frequency of electromagnetic waves, depending on the interference caused by the periodic arrays of both dielectric and conducting materials which makes a frequency selective response [7]–[9]. FSSs, in general, have many common shapes and geometries, such as a SL, ring, dipole, cross dipole, Jerusalem cross, and tripole. These types can be in one of four modes; high-pass, low-pass, band-pass, and band stop filter [9]. Most of the previous studies showed that the SL FSS has the best performance and stability to work within the angular sensitivity, cross polarization transverse electric (TE) or transverse magnetic (TM) modes, and small band separation [10]. Thus, the SL FSS shape has been selected for this study.

In order to test SL FSS, ECM has been considered as the simple method. The first usage of ECM technique and first applied to frequency selective circuits was by Anderson [11]. The advantage of ECM is that it can quickly characterize the FSS response with varying element dimensions. On the other hand, ECM cannot be used to predict the performance of sophisticated shapes other than simple shapes like SL FSS [12].

The frequency response in SL FSS is determined by the element dimensions (p , d , s , g), as shown in Figure 1. Where p is the separation period, d is the dimension of the loop, s is the width of the conducting strip, and g is inter-element spacing. These parameters determine the location of the f_r (resonant frequency). The parameter g controls the FSS angular performance [13]. Previous studies have suggested that a bigger SL in size is generally effective at a lower f_r and a smaller g ensures stable f_r with varying incidence angles [14].

ECM technique imposes that the interaction between incident wave and the FSS is represented as a wave propagating through a transmission line, with shunt lumped circuit impedances. The shunt impedance could be inductive or capacitive relying on whether the polarization of the incident signal is parallel or perpendicular to the strip. As shown in Figure 2, the two adjacent strips are approximated as one strip with width (w) equal to ($2s$) [15]. The normalized shunt inductive reactance expression of the inductive strip was given as in [16]:

$$X_{TE} = \frac{\omega_o L}{z_o} = \frac{p \cos(\theta)}{\lambda} \left[\ln \left(\csc \left(\frac{\pi w}{2p} \right) \right) + G(p, w, \lambda, \theta) \right] \quad (1a)$$

$$X_{TM} = \frac{p \sec \phi}{\lambda} \left[\ln \left(\csc \left(\frac{\pi w}{2p} \right) \right) + G(p, w, \lambda, \phi) \right] \quad (1b)$$

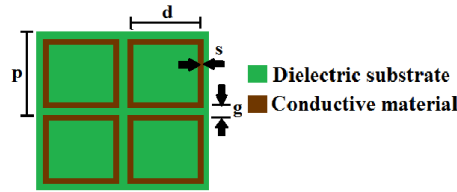


Figure 1. Array of SL FSS elements

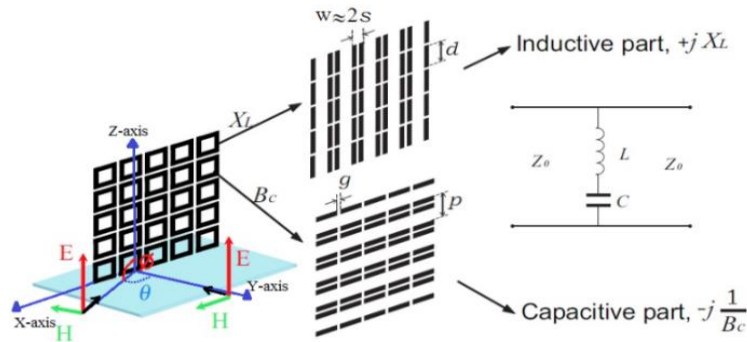


Figure 2. Inductive and capacitive part of the SL FSS shape [9]

The normalized shunt capacitive susceptance expression was given as in (2) [12] by Lee:

$$B_{TE} = \frac{\omega_o C}{Y_o} = \frac{4p \sec(\theta)}{\lambda} \left[\ln \left(\csc \left(\frac{\pi g}{2p} \right) \right) + G(p, g, \lambda, \theta) \right] \epsilon_{eff} \tag{2b}$$

$$B_{TM} = 4F(p, g, \lambda) = \frac{4p \cos \phi}{\lambda} \left[\ln \left(\csc \left(\frac{\pi g}{2p} \right) \right) + G(p, g, \lambda, \phi) \right] \epsilon_{eff} \tag{2b}$$

where G is the correction term:

$$G(p, w, \lambda, \theta) = \frac{0.5(1-\beta^2)^2 \left[\left(1 - \frac{\beta^2}{4}\right)(A_{1+} + A_{1-}) \right] + 4\beta^2 A_{1+} A_{1-}}{\left(1 - \frac{\beta^2}{4}\right) + \beta^2 \left(1 + \frac{\beta^2}{2} - \frac{\beta^4}{8}\right)(A_{1+} + A_{1-}) + 2\beta^6 A_{1+} A_{1-}} \tag{3a}$$

$$G(p, g, \lambda, \theta) = \frac{0.5(1-\beta^2)^2 \left[\left(1 - \frac{\beta^2}{4}\right)(A_{1+} + A_{1-}) \right] + 4\beta^2 A_{1+} A_{1-}}{\left(1 - \frac{\beta^2}{4}\right) + \beta^2 \left(1 + \frac{\beta^2}{2} - \frac{\beta^4}{8}\right)(A_{1+} + A_{1-}) + 2\beta^6 A_{1+} A_{1-}} \tag{3b}$$

where

$$A_{1\pm}^{TE} = \frac{1}{\sqrt{\left(\frac{p \sin \theta}{\lambda} \pm 1\right)^2 - \frac{p^2}{\lambda^2}}} - 1 \tag{4a}$$

$$A_{1\pm}^{TM} = \frac{1}{\sqrt{1 - \frac{p^2 \cos^2 \theta}{\lambda^2}}} - 1 \tag{4b}$$

and

$$\beta = \sin(0.5\pi w/p) \tag{5a}$$

or

$$\beta = \sin\left(\frac{0.5\pi g}{p}\right) \tag{5b}$$

where $Z_o = 377 \Omega$, θ is the incidence angle, λ is the wavelength in air at operating frequency, w is equal to $2s$ in this calculation, and ϵ_{eff} is the effective permittivity of the surrounding dielectric substrate that influences the capacitance value.

Equations, which are presented in this section, have shown that the FSS response is a function of SL element dimensions, incidence angles, and the dielectric material which holds and gives support for the FSS. In addition, these equations are valid for $[p(1 + \sin\theta) < \lambda]$ for TE wave incidence and $[p(\cos\theta) < \lambda]$ for TM wave incidence for a given range of incidence angle. The equivalent impedance of the SL FSS is given by (6):

$$Z_{FSS} = j \left(X_L - \frac{1}{B_c} \right) \tag{6}$$

Hence, the normalized impedance (Z_n) for the transmission line circuit, as illustrated in Figure 3, can be determined by (7):

$$Z_n = \frac{Z_{FSS}}{Z_o} = j \left(\frac{X_L}{Z_o} - \frac{1}{B_c Z_o} \right) = j \left(\frac{X_L}{Z_o} - \frac{Y_o}{B_c} \right) \tag{7}$$

By using the *ABCD* matrix, the transmission and reflection coefficients for the SL FSS can be determined. As it is known that an *ABCD* matrix can represent any given network; based on the *ABCD* parameters, the transmission coefficient (S_{21}) and the reflection coefficient (S_{11}) can be determined [17]. For example, for a T-network as illustrated in Figure 3, the *ABCD* matrix is presented by (8):

$$\begin{bmatrix} A & B \\ C & D \end{bmatrix} = \begin{bmatrix} 1 + \frac{Z_1}{Z_3} & Z_1 + Z_2 + \frac{Z_1 Z_2}{Z_3} \\ \frac{1}{Z_3} & 1 + \frac{Z_2}{Z_3} \end{bmatrix} \tag{8}$$

The scattering S-matrix is defined as (9):

$$\begin{bmatrix} S_{11} & S_{12} \\ S_{21} & S_{22} \end{bmatrix} = \begin{bmatrix} \frac{A+B-C-D}{\Delta} & \frac{2(AD-BC)}{\Delta} \\ \frac{2}{\Delta} & \frac{-A+B-C+D}{\Delta} \end{bmatrix} \tag{9}$$

where $\Delta = A + B + C + D$. For the SL FSS, $Z_1 = Z_2 = 0$ and $Z_3 = Z_n$ as defined in (9). Therefore, based on (10) and (11), the transmission coefficient S_{21} and reflection coefficient S_{11} for the FSS can be evaluated. Because of symmetry $S_{11} = S_{22}$ and $S_{12} = S_{21}$. The *ABCD* matrix can be expressed as a function of S_{21} and S_{11} as (10), (11):

$$S_{21} = \frac{2}{A+B+C+D} = \frac{2}{1+0+\frac{1}{Z_3}+1} = \frac{2}{2+\frac{1}{Z_3}} = \frac{2}{2+Y} = T \tag{10}$$

$$S_{11} = \Gamma = 1 - |T|^2 = 1 - \frac{4}{4+Y^2} \tag{11}$$

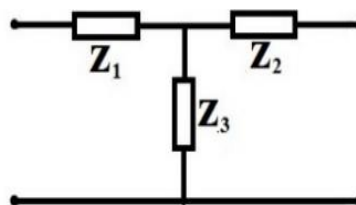


Figure 3. Transmission line which can be represented by *ABCD* matrix

2.2. Large-scale PLMs

Large-scale PLMs estimate the attenuation over distance of propagation signals and are vital for designing communication systems. Different types (deterministic, empirical, and stochastic) of large-scale PLMs exist, but a measurement-based PLM provides realistic insight into the propagation characteristics of a

wireless channel [6]. Two types of PLMs are studied in this paper: CI and FI. The CI PLM is defined by the path loss exponent (PLE) n [18]–[21]:

$$PL^{CI}(f, d) [dB] = FSPL(f, d_o) + 10n \log_{10} \left(\frac{d}{d_o} \right) + X_{\sigma}^{CI} \quad (12)$$

$$FSPL(f, d_o) = 10 \log_{10} \left(\frac{4\pi f d_o}{\lambda} \right)^2 \quad (13)$$

where λ is the wavelength in m, $d_o=1$ m, and X_{σ}^{CI} is a zero mean Gaussian random variable with standard deviation σ^{CI} given by (14) and (15) [6]:

$$X_{\sigma}^{CI} = PL^{CI}[dB] - FSPL(f, d_o)[dB] - 10n \log_{10}(d) = A - nD \quad (14)$$

$$\sigma^{CI} = \sqrt{\sum \frac{X_{\sigma}^{CI2}}{N}} = \sqrt{\sum \frac{(A-nD)^2}{N}} \quad (15)$$

where $A = PL^{CI}(f, d)[dB] - FSPL(f, d_o)[dB]$, $D = 10 \log_{10}(d)$, and N is the number of measured PL data points. The CI PLM uses a physically based reference distance, d_o , and n is the mean PLE, which indicates how fast PL increases with distance. The FI PLM is currently used in standards work, such as the 3rd Generation partnership project (3GPP), and can be calculated as (6) [22]–[25]:

$$PL^{FI}(d)[dB] = \alpha + 10\beta \log_{10} d + X_{\sigma}^{FI} \quad (16)$$

Assume that $B = PL^{FI}(d) [dB]$ and the zero mean Gaussian random variable is [6]:

$$X_{\sigma}^{FI} = B - \alpha - \beta D \quad (17)$$

and the standard deviation σ^{FI} is [6]:

$$\sigma^{FI} = \sqrt{\sum \frac{X_{\sigma}^{FI2}}{N}} = \sqrt{\sum \frac{(B-\alpha-\beta D)^2}{N}} \quad (18)$$

where α is the floating intercept and given by [6]:

$$\alpha = \frac{\sum D \sum B D - \sum D^2 \sum B}{(\sum D)^2 - N \sum D^2} \quad (19)$$

and β is the slope of the line (different than the PLE) and given by (20) [6]:

$$\beta = \frac{\sum D \sum B - N \sum D B}{(\sum D)^2 - N \sum D^2} \quad (20)$$

where X_{σ}^{FI} is a log-normal random variable with mean 0 dB and standard deviation σ^{FI} .

3. RESULTS AND DISCUSSION

3.1. SL FSS (MATLAB)

MATLAB has been used to solve the theoretical equations for ECM for the suggested design of the SL FSS element; resonance occurs when each half loop acts as a dipole [4,9]. The basic rule of thumb in designing loop circumference is to make its response approximately equal to the resonant frequency (61.5 GHz). Basic design rules for SL FSS element dimensions are given along with equations for the ECM. Where its dimensions are: $p=1.4$ mm, $s=0.1$ mm, $d=1.2$ mm, $g=0.2$ mm, and $\epsilon_{eff} = \frac{\epsilon_r+1}{2} = 2$. Figures 4 and 5 show the S_{21} and S_{11} responses coefficients for the designed SL FSS at a 0° incidence angle, respectively.

3.2. SL FSS (CST studio suite)

CST Studio Suite is used to test and analyze the designed SL FSS parameters. The analyzes method used is the finite integration technique on Cartesian or tetrahedral grids. As shown in Figure 6, SL FSS has been tested for a range of different incidence angles from 0° to 60° . The S_{21} is presented for both TE and TM

modes, as shown in Figures 7 and 8, respectively. The S_{11} is also presented for the TE and TM modes, as shown in Figures 9 and 10, respectively. All of the figures for the transmission and reflection coefficients are expressed in a range of frequencies from 50 to 70 GHz. Copper with a 0.07 mm thickness is used as the conductive material. The dielectric material is Arlon AD 300, which has a 0.1 mm thickness and a relative permittivity value of 3.

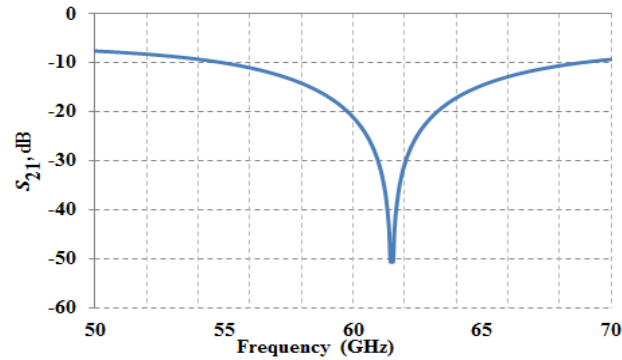


Figure 4. The theoretical frequency transmission response of SL FSS wallpaper based on ECM equations

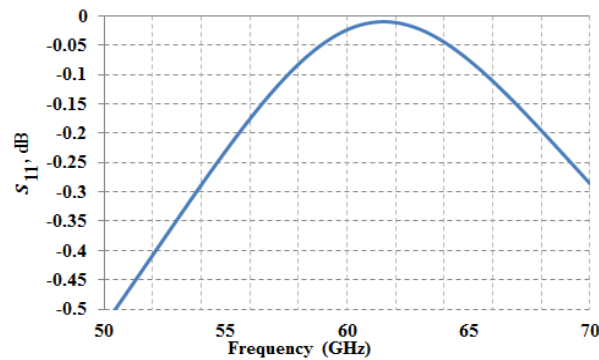


Figure 5. The theoretical frequency reflection response of SL FSS wallpaper based on ECM equations

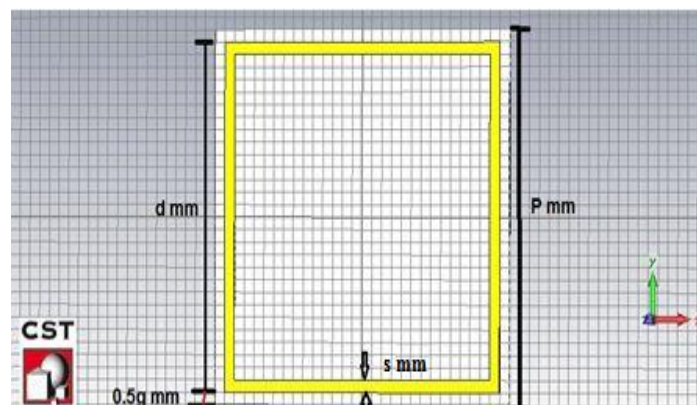


Figure 6. The SL FSS dimensions, where $p = 1.4$ mm, $g = 0.2$ mm, $d = 1.2$ mm, and $s = 0.1$ mm

In order to evaluate the response of a filter as a band-stop, the attenuation value must exceed -25 dB at the resonant frequency (61.5 GHz) to kill the signal [9]. As shown in Figures 7 and 8, the transmission coefficients for both TE and TM modes are more than -25 dB. That means that the signal will be dead when

trying to penetrate the area of interest. The reflection coefficients shown in Figures 9 and 10 are also smaller than -0.05 dB at 61.5 GHz, which allows the SL FSS wallpaper to act as a perfect reflector inside the area of interest, achieving its goal.

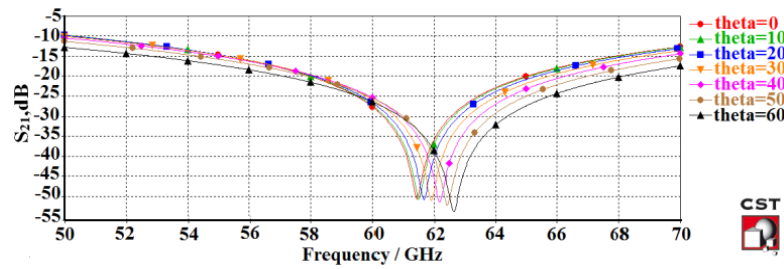


Figure 7. The transmission response of SL FSS wallpaper for TE-mode

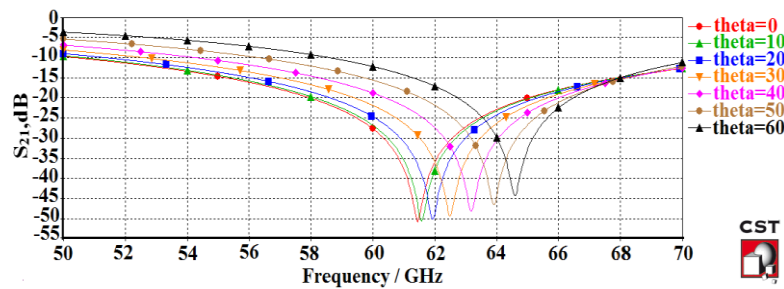


Figure 8. The transmission response of SL FSS wallpaper for TM-mode

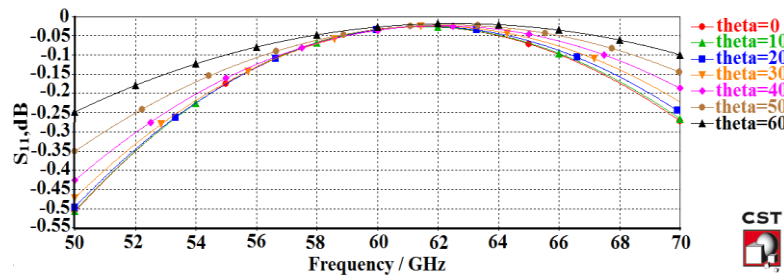


Figure 9. The reflection response of SL FSS wallpaper for TE-mode

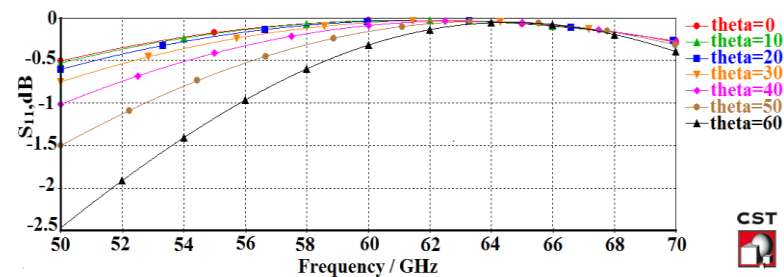


Figure 10. The reflection response of SL FSS wallpaper for TM-mode

3.3. Investigation of scenarios using ‘wireless InSite’

‘Wireless InSite’ is used as a tool to evaluate the received power for different scenarios inside the area of interest. The reflection and transmission coefficient values of the SL FSS wallpaper have been

exported to ‘Wireless InSite’ in order to obtain the SL FSS wallpaper response. The scenario of interest in a room with dimension 15×10 m has been investigated. The target scenario investigates a MIMO communication system with/without SL FSS wallpaper, while MIMO scenario studies two more sub-scenarios; with/without human bodies.

3.3.1. MIMO system scenario

a. MIMO without SL FSS wallpaper

This scenario contains a 2x2 MIMO communication system for Tx and the Rx’s. Both the Tx and Rx’s are assumed to consist of two antenna elements spaced by $\lambda/2$ [26]. Tx has a directional antenna with 10 dBm input power, 14 dBi gain, 2.5 m height, and 90° HPBW. Rx’s are distributed in 20 locations. Each Rx has an omnidirectional antenna with a sensitivity of -64 dBm and 1.5 m height.

1) Without human bodies

The 2D and 3D views of this scenario are shown in Figures 11 and 12. Table 1 shows the electrical parameters of the materials used in this study [9]. Figure 12 shows the 3D view of the first scenario, which has been studied without using SL FSS wallpaper. The received signal power at each Rx location is shown in Figure 13.

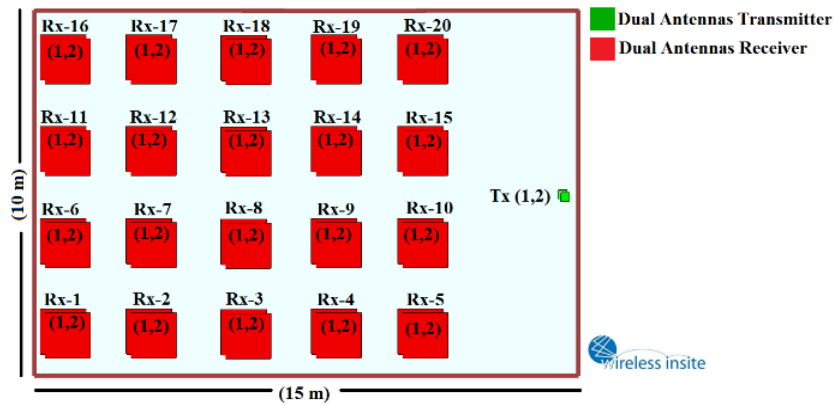


Figure 11. 2D view for the MIMO scenario

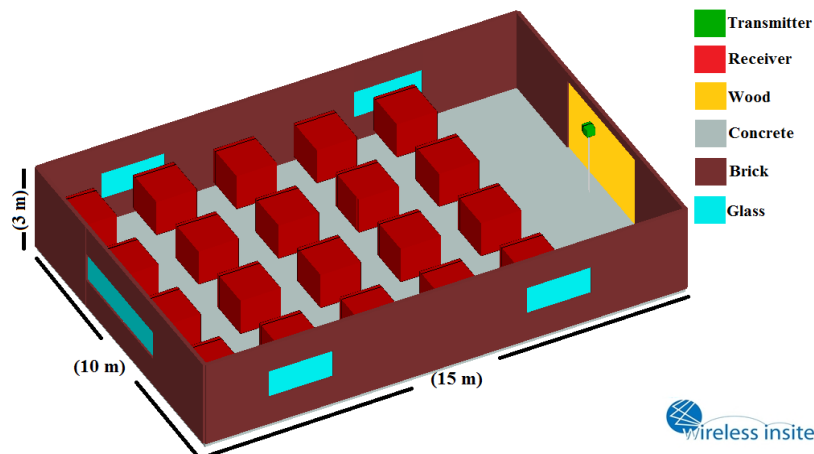


Figure 12. 3D view for the MIMO scenario without SL FSS wallpaper and human bodies

Table 1. Electrical parameters used for building area of interest [9]

Component	Material	Conductivity, σ (S/m)	Relative Electrical Permittivity, ϵ_r	Thickness (m)
Walls	Brick	0.001	4.44	0.150
Ceiling and Floor	Concrete	0.015	15	0.3
Windows	Glass	0	2.4	0.003
Doors	Wood	0	5	0.03

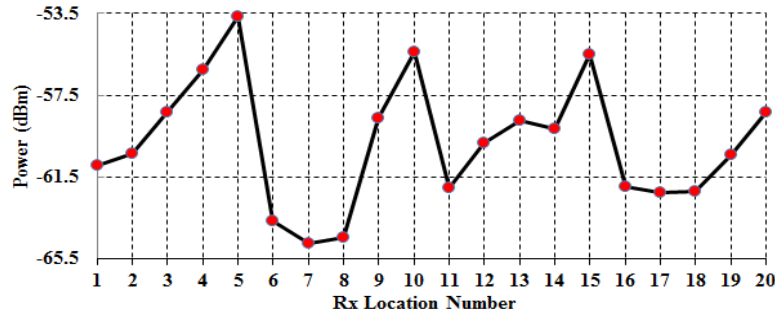


Figure 13. The received signal power for each Rx location number for the MIMO system scenario without SL FSS wallpaper and human bodies

2) With human bodies

The 2D and 3D views of this scenario are shown in Figures 14 and 15. The black parallelepipeds represent the number of human bodies situated randomly in the room. The human body has been modelled inside ‘Wireless InSite’ based on the complex permittivity values of its basic components; skin, fat, muscle, and pure water, at a 60 GHz resonant frequency, as summarized in Table 2 [4]. The received power at each Rx location is shown in Figure 16. Figure 17 shows that the average received power in the MIMO system has been attenuated by 3 dB, on average, with the presence of human bodies.

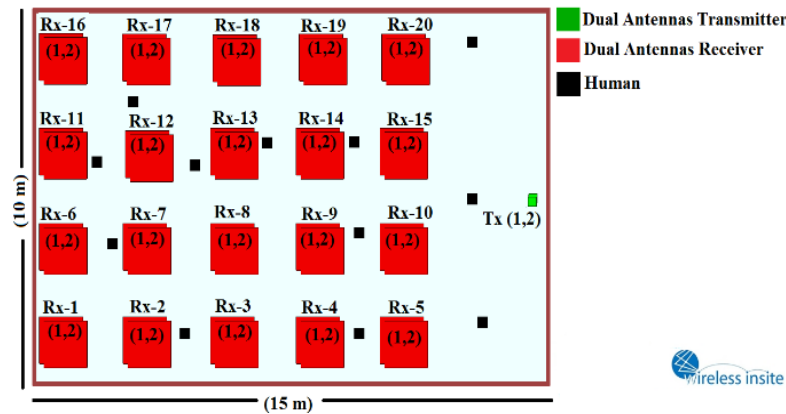


Figure 14. 2D view for the MIMO scenario without SL FSS, but with a number of human bodies

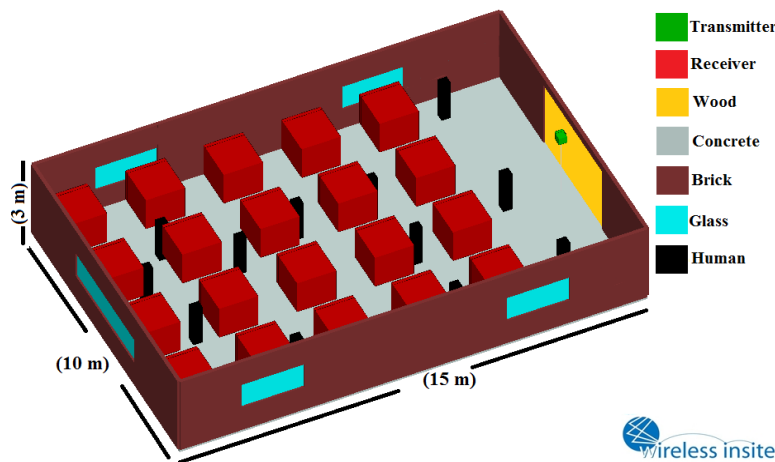


Figure 15. 3D view for the MIMO scenario without SL FSS wallpaper, but with a number of human bodies

Table 2. Complex permittivity at 60 GHz of human body components [4]

Human tissues	ϵ_c
Skin	$7.98 - j10.91$
Fat	$2.51 - j0.84$
Muscle	$12.85 - j15.74$
Pure Water (20 °C)	$11.9 - j19.5$

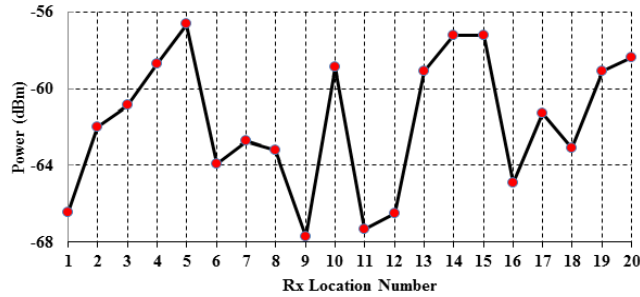


Figure 16. The received signal power for each Rx location number for the MIMO system scenario without SL FSS wallpaper, but with a number of human bodies

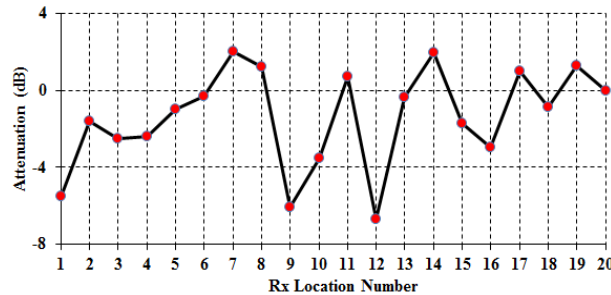


Figure 17. The received signal power for each Rx location number for the MIMO system scenario without SL FSS wallpaper, but with a number of human bodies

b. MIMO with SL FSS wallpaper
 1) Without human bodies

The scenario depicted in Figure 12 is replicated by employing the technique of attaching SL FSS wallpaper at a distance of $\lambda/10$ from the wall. It is demonstrated in Figure 18. A representation of the received signal power at each Rx site is shown in Figure 19.

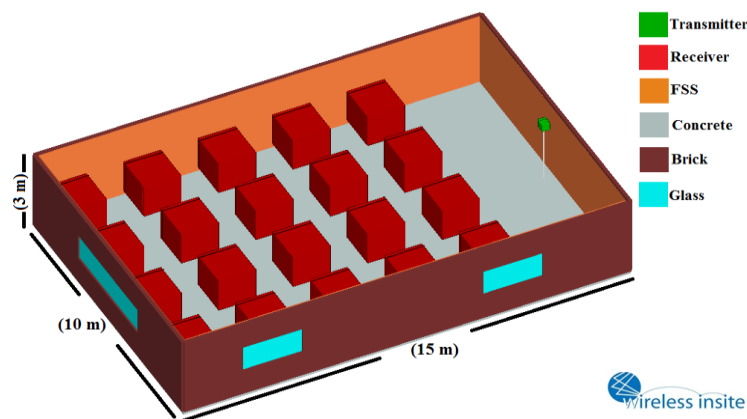


Figure 18. 3D view for the MIMO scenario with SL FSS wallpaper, but without human bodies

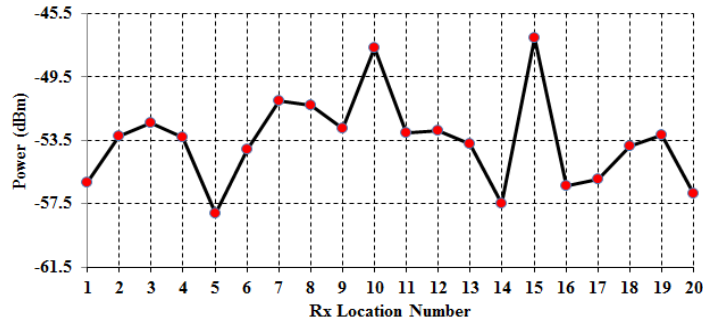


Figure 19. The received signal power for each Rx location number for the MIMO system scenario with SL FSS wallpaper, but without human bodies

2) With human bodies

Figure 20 shows the above scenario with a number of human bodies added. Figure 21 shows the received signal power at each Rx location. Figure 22 shows that the received power has been reduced in the MIMO system scenario with SL FSS wallpaper and a number of human bodies by an average of 2 dB compared to the scenario without human bodies.

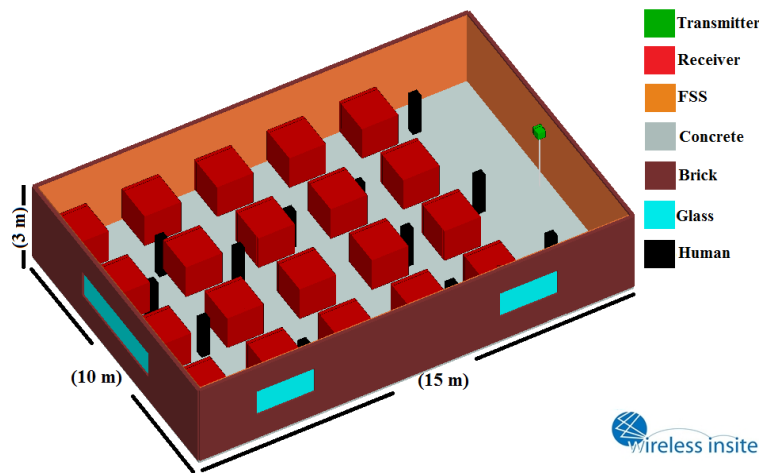


Figure 20. 3D view for the MIMO scenario with SL FSS wallpaper and a number of human bodies

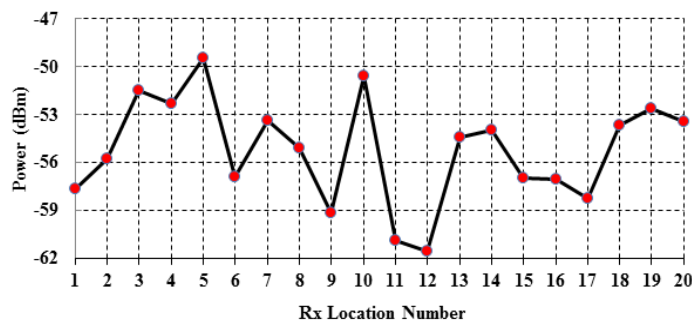


Figure 21. The received signal power for each Rx location number for the MIMO system scenario with SL FSS wallpaper and a number of human bodies

Figures 23 and 24 show the difference in the received signal power before and after attaching SL FSS wallpaper at each Rx location for the MIMO system scenario with/without human bodies, respectively.

In these figures, the received power at each Rx location has been enhanced after attaching SL FSS wallpaper by an average of 6.87 dB with and 6.53 dB without human bodies. Note that the received power at Rx location number 5, as shown in Figure 23, has been attenuated due to the beam-width of the Tx, whose signal suffers more reflections before reaching the Rx.

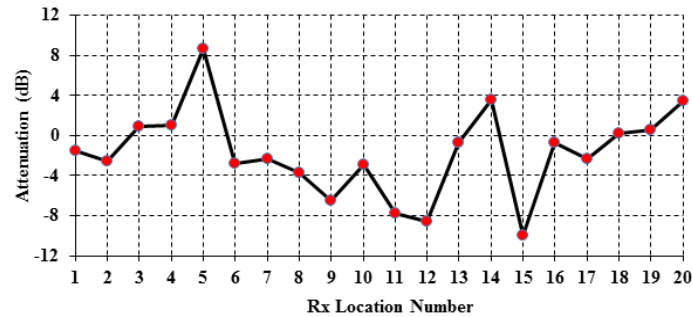


Figure 22. The achieved attenuation for each Rx location number for MIMO system scenario with SL FSS wallpaper with/without human bodies

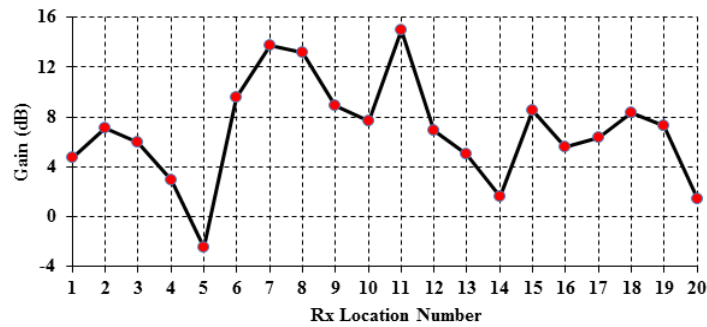


Figure 23. The gain enhancement for each Rx location number between MIMO system scenarios with/without SL FSS wallpaper with human bodies

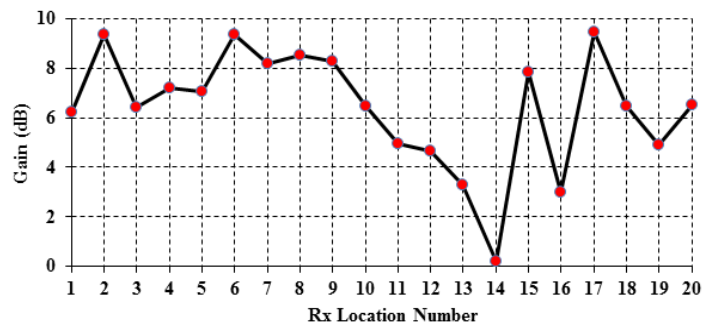


Figure 24. The gain enhancement for each Rx location number between MIMO system scenarios with/without SL FSS wallpaper without human bodies

3.4. Large-scale PLMs

Using the two large-scale propagation PLMs presented in subsection 2.2 and the indoor simulation data for a 60 GHz band, PL parameters are analysed and compared. The single-frequency CI and FI PLMs parameters at a 60 GHz band for different indoor scenarios are presented in Table 3 (for the purpose of comparing PLMs and saving space, only directional antenna for Tx and omnidirectional antenna for Rx PL data captured with vertically-polarized (V-V) Tx and Rx antennas are included). It can be observed from Table 3 that the CI model provides intuitive PLM parameter values due to its physical basis, while the

parameters in the FI model sometimes contradict fundamental principles. For example, for the humans without SL FSS wallpaper scenario in a non-line-of-sight (NLOS) environment, the CI model generates a PLE of 3.39, which nearly matches the theoretical free-space NLOS PLE of 4; however, in the FI model, it is -0.02, meaning that the PL decreases with distance, which is obviously not reasonable or physically possible in a passive channel.

The resulting single-frequency path loss model parameters emphasize the frequency dependence of indoor PL beyond the first meter of free space path loss (FSPL), where PLEs in the ring FSS wallpaper without humans scenarios at 61.5 GHz are larger than the PLEs for the same scenarios, but without ring FSS wallpaper, as shown in Table 3. Specifically, line-of-sight (LOS) PLEs are 1.46 and 1.7 at 61.5 GHz with/without ring FSS wallpaper in without humans scenarios, respectively, indicating constructive interference and waveguiding effects in LOS indoor channels at mm-wave frequencies. Furthermore, the NLOS PLEs are 3.4 and 2.9 at 61.5 GHz for the same scenarios, respectively, showing that 61.5 GHz propagating waves attenuate by 10 dB more per meter of distance in the indoor environment beyond the first meter, as provided in Table 3. For with/without ring FSS wallpaper with humans scenarios, LOS PLEs are 1.5 and 1.76 at 61.5 GHz, respectively, indicating constructive interference and waveguiding effects in LOS indoor channels at mm-wave frequencies. Furthermore, the same reasons apply to the NLOS PLEs, which are 3 and 3.9 at 61.5 GHz for the same scenarios, respectively. By using the strongest NLOS received power path from Tx-Rx (NLOS-Best) PLE reduced to 2.54 and 2.9, which is an important improvement for NLOS case.

Table 3. Parameters for the single-frequency CI and FI PLMs in a typical modified indoor scenario

Scenario	Pol.	Freq. (GHz)	Env.	Distance Range (m)	Model	PLE/ β	α [dB]	σ [dB]				
SL FSS Wallpaper with Humans	V-V	61.5	LOS	4-14.31	CI	1.5	-	2.68				
					FI	0.79	74.8	2.4				
				NLOS	CI	3	-	6.4				
					FI	0.79	99	3.2				
			NLOS-Best	4-14.31	CI	2.54	-	4.2				
					FI	0.33	89	1.8				
				LOS	4-14.31	CI	1.46	-	2.2			
						FI	0.76	74	2			
SL FSS Wallpaper without Humans	V-V	61.5	LOS	4-14.31	CI	1.46	-	2.2				
					FI	0.76	74	2				
				NLOS	4-14.31	CI	2.9	-	6.13			
						FI	-0.16	98	2.6			
			NLOS-Best	4-14.31	CI	2.5	-	4.2				
					FI	0.21	90.5	1.2				
				Humans without SL FSS Wallpaper	V-V	61.5	LOS	4-14.31	CI	1.76	-	3
									FI	1	75.37	2.74
NLOS	4-14.31	CI	3.39				-	7.22				
		FI	-0.02				101.28	3.87				
NLOS-Best	4-14.31	CI	2.9	-	5.87							
		FI	0.15	95	3.34							
	Without Humans and SL FSS Wallpaper	V-V	61.5	LOS	4-14.31	CI	1.7	-	2			
						FI	1.36	74	2			
NLOS					4-14.31	CI	3.4	-	6.88			
						FI	0.01	98	3.5			
NLOS-Best				4-14.31	CI	3	-	5.6				
					FI	-0.01	90.5	2.24				

The FI model indicates lower attenuation as a function of log-distance in some cases (human without ring FSS wallpaper LOS $\beta=1$, compared to $n=1.76$, and NLOS $\beta=-0.02$, compared to $n=3.39$). However, the FI model parameters can exhibit strange, non-physics-based values, specifically, when β is negative, which implies ultra-low loss with distance (less than in a waveguide), which does not follow basic physics. We use $d_o=1$ m in mm-wave PLMs since base stations will be shorter or mounted indoors and closer to obstructions [23]. The physically-based 1 m FSPL anchor of the CI model for single-frequencies allows for a simpler model (only one parameter) with virtually no decrease in model accuracy by representing free-space propagation close to the transmitting antenna. Therefore, the more physically sound and simpler CI model with a 1 m free space-reference distance term is more convenient to use to model indoor mm-wave channels. Figure 25 shows scatter plots for CI PLM parameters inside modified indoor environments for different scenarios as shown in: Figure 25(a) for SL FSS wallpaper with humans, Figure 25(b) for SL FSS wallpaper without humans, Figure 25(c) for humans without SL FSS wallpaper, and Figure 25(d) for a scenario without humans and SL FSS wallpaper, for co-polarized antennas at Tx, 20 LOS, and 122 NLOS readings.

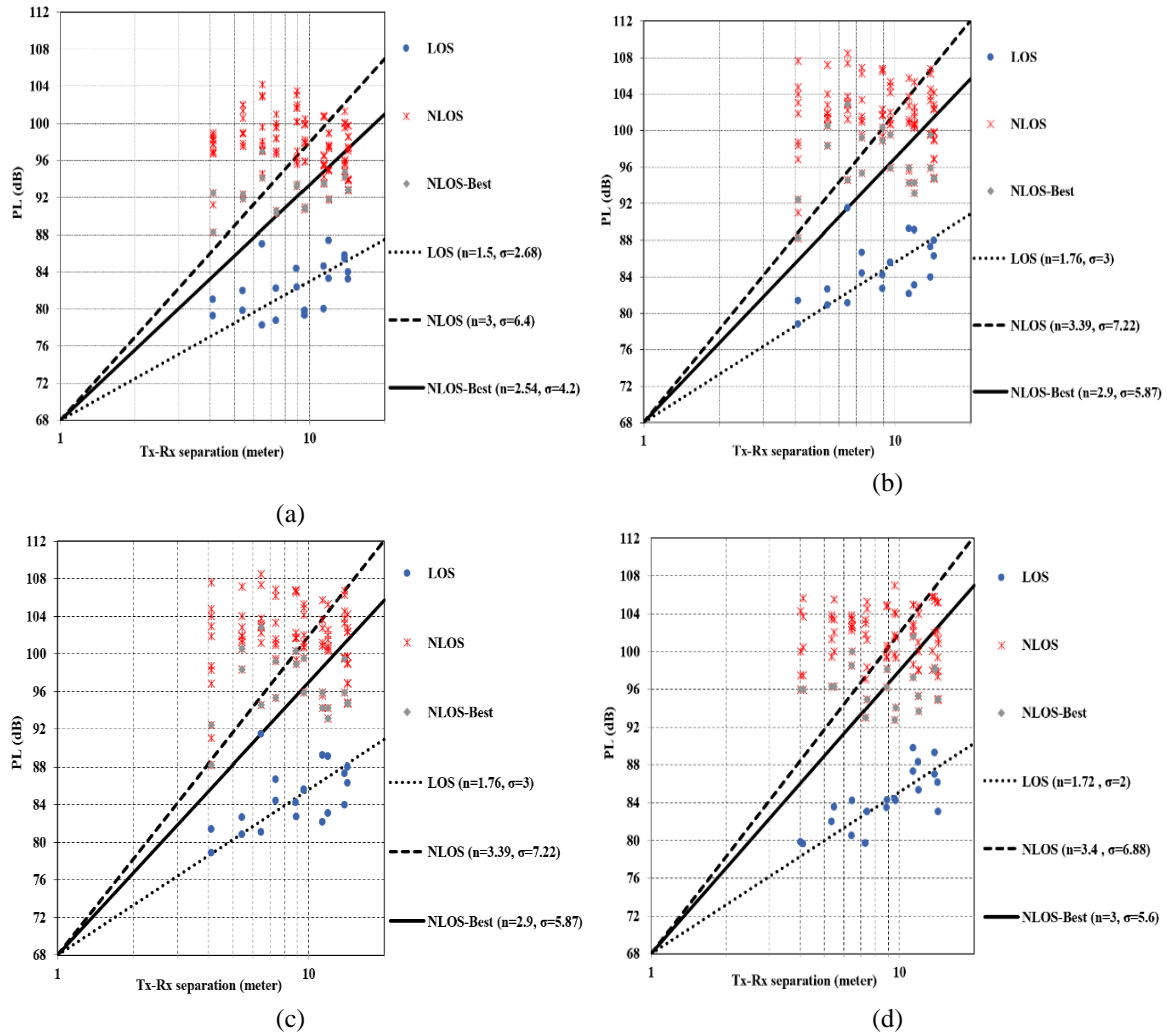


Figure 25. Single-frequency (61.5 GHz) CI ($d_0 = 1$ m) PLM parameters scatter plot for Tx at a height of 2.5 m, and Rx antennas height of 1.5 m in an atypical modified indoor office environment for co-polarized antennas: (a) SL FSS wallpaper with humans, (b) SL FSS wallpaper without humans, (c) humans without SL FSS wallpaper, and (d) without humans and SL FSS wallpaper

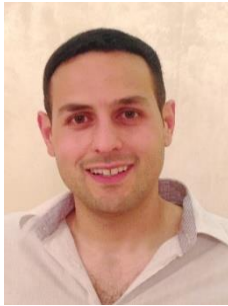
4. CONCLUSION




In order to enhance the performance of indoor 60 GHz wireless networks as a case study multiple input multiple output (MIMO) system, SL FSS has been selected because the propagation of 60 GHz can be easily blocked by obstacles or humans. Results showed that received signal power had been enhanced by an average of 6.87 dB for MIMO system. However, the presence of human bodies attenuated the strength of the received signal power by an average of 2.5 dB, and decreased the capacity of system. While using SL FSS wallpaper, the capacity for MIMO system generally will be enhanced, which proved that the presence of SL FSS wallpaper in an indoor environment increased the strong reflected wave components in each Rx location.

This paper also described mm-wave propagation simulations in modified indoor scenarios at 61.5 GHz and presented and compared the single-frequency FI and CI PLMs. Single-frequency path loss results showed that the CI model is preferable to the FI model (presently used in 3GPP) for modified indoor environments due to its physical basis, simplicity, and robustness over measured frequencies and distance ranges. The CI model is physically tied to the TX power using a close-in free space reference and standardized measurements around an inherent 1 m free space reference distance that is physically based. Thus, it is easy to use for varying distances since it involves the use of a single parameter (PLE, or n).




REFERENCES

- [1] M. Alkhatra and N. Qasem, "Improving and extending indoor connectivity using relay nodes for 60 GHz applications," *International Journal of Advanced Computer Science and Applications*, vol. 7, no. 4, pp. 427–434, 2016, doi: 10.14569/IJACSA.2016.070456.
- [2] M. Kim, A. Ghosh, R. Takahashi, and K. Shibata, "Indoor channel measurement at 300 GHz and comparison of signal propagation with 60 GHz," *IEEE Access*, vol. 11, pp. 124040–124054, 2023, doi: 10.1109/ACCESS.2023.3330653.
- [3] D. Zelenchuk, V. Kirillov, C. Kärnfelt, F. Gallée, and I. Munina, "Metamaterial-based LTCC compressed Luneburg lens antenna at 60 GHz for wireless communications," *Electronics*, vol. 12, no. 11, May 2023, doi: 10.3390/electronics12112354.
- [4] N. Qasem, E. A. Aldorgam, and H. Y. Alzou'bi, "Overcoming the influence of human shadowing and obstacles via modified building using frequency selective wallpapers for 60 GHz," *Journal of Communication and Computer*, vol. 13, no. 2, Feb. 2016, doi: 10.17265/1548-7709/2016.02.004.
- [5] H. Azzahafi, M. El Yahyaoui, A. El Moussati, G. El Zein, and A. Garcia Armada, "Enhanced 4×4 MIMO RoF architecture for 5G mmWave indoor applications at 60 GHz unlicensed band," *Optics Communications*, vol. 533, Apr. 2023, doi: 10.1016/j.optcom.2023.129266.
- [6] G. R. Maccartney, T. S. Rappaport, S. Sun, and S. Deng, "Indoor office wideband millimeter-wave propagation measurements and channel models at 28 and 73 GHz for ultra-dense 5G wireless networks," *IEEE Access*, vol. 3, pp. 2388–2424, 2015, doi: 10.1109/ACCESS.2015.2486778.
- [7] N. Qasem, "Enhancing the capacity of the Indoor 60 GHz band via modified indoor environments using ring frequency selective surface wallpapers and path loss models," *International Journal of Electrical and Computer Engineering (IJECE)*, vol. 8, no. 5, pp. 3003–3020, Oct. 2018, doi: 10.11591/ijece.v8i5.pp3003-3020.
- [8] U. Rafique, S. A. Ali, M. T. Afzal, and M. Abdin, "Bandstop filter design for GSM shielding using frequency selective surfaces," *International Journal of Electrical and Computer Engineering (IJECE)*, vol. 2, no. 6, pp. 846–850, Dec. 2012, doi: 10.11591/ijece.v2i6.1820.
- [9] N. Qasem, "Enhancing wireless communication system performance through modified indoor environments," Doctoral Thesis, Loughborough University, 2014.
- [10] T. K. Wu, "Frequency selective surfaces," in *Encyclopedia of RF and Microwave Engineering*, Hoboken, NJ, USA: Wiley, 1995.
- [11] I. Anderson, "On the theory of self-resonant grids," *Bell System Technical Journal*, vol. 54, no. 10, pp. 1725–1731, Dec. 1975, doi: 10.1002/j.1538-7305.1975.tb03551.x.
- [12] C. K. Lee and R. J. Langley, "Equivalent-circuit models for frequency-selective surfaces at oblique angles of incidence," *IEE Proceedings H Microwaves, Antennas and Propagation*, vol. 132, no. 6, 1985, doi: 10.1049/ip-h-2.1985.0070.
- [13] C. Tsakonas, C. Mias, and C. Oswald, "An investigation into feasibility of designing frequency-selective windows employing periodic structures, final report for the radiocommunications agency," 2006.
- [14] B. Munk, *A frequency selective surfaces: theory and design*. John Wiley & Sons, 2005.
- [15] S. M. A. Hamdy and E. A. Parker, "Current distribution on the elements of a square loop frequency selective surface," *Electronics Letters*, vol. 18, no. 14, 1982, doi: 10.1049/el:19820427.
- [16] N. Marcuvitz, *Waveguide handbook*. McGraw Hill, 1951.
- [17] D. Dawod and N. Qasem, "Enhancing the capacity of MIMO systems via modified building using Frequency Selective wallpapers," in *2015 6th International Conference on Information and Communication Systems (ICICS)*, Apr. 2015, pp. 171–176, doi: 10.1109/IACS.2015.7103222.
- [18] G. R. MacCartney, S. Deng, and T. S. Rappaport, "Indoor office plan environment and layout-based mmWave path loss models for 28 GHz and 73 GHz," in *2016 IEEE 83rd Vehicular Technology Conference (VTC Spring)*, May 2016, pp. 1–6, doi: 10.1109/VTCSpring.2016.7504287.
- [19] M. J. Feuerstein, K. L. Blackard, T. S. Rappaport, S. Y. Seidel, and H. H. Xia, "Path loss, delay spread, and outage models as functions of antenna height for microcellular system design," *IEEE Transactions on Vehicular Technology*, vol. 43, no. 3, pp. 487–498, 1994, doi: 10.1109/25.312809.
- [20] M. A. Samad, S.-W. Choi, C.-S. Kim, and K. Choi, "Wave propagation modeling techniques in tunnel environments: a survey," *IEEE Access*, vol. 11, pp. 2199–2225, 2023, doi: 10.1109/ACCESS.2022.3233877.
- [21] M. A. Samad, D.-Y. Choi, H. Son, and K. Choi, "Analysis of centimeter and millimeter-wave path loss at emergency exit," *IEEE Access*, vol. 11, pp. 34217–34226, 2023, doi: 10.1109/ACCESS.2023.3264648.
- [22] G. R. MacCartney, M. K. Samimi, and T. S. Rappaport, "Omnidirectional path loss models in New York City at 28 GHz and 73 GHz," in *2014 IEEE 25th Annual International Symposium on Personal, Indoor, and Mobile Radio Communication (PIMRC)*, Sep. 2014, pp. 227–231, doi: 10.1109/PIMRC.2014.7136165.
- [23] T. S. Rappaport, G. R. MacCartney, M. K. Samimi, and S. Sun, "Wideband millimeter-wave propagation measurements and channel models for future wireless communication system design," *IEEE Transactions on Communications*, vol. 63, no. 9, pp. 3029–3056, Sep. 2015, doi: 10.1109/TCOMM.2015.2434384.
- [24] L. Rubio *et al.*, "Millimeter-wave channel measurements and path loss characterization in a typical indoor office environment," *Electronics*, vol. 12, no. 4, Feb. 2023, doi: 10.3390/electronics12040844.
- [25] A. A. Budalal and M. R. Islam, "Path loss models for outdoor environment-with a focus on rain attenuation impact on short-range millimeter-wave links," *e-Prime - Advances in Electrical Engineering, Electronics and Energy*, vol. 3, Mar. 2023, doi: 10.1016/j.prime.2023.100106.
- [26] N. Bisht, P. K. Malik, S. Das, T. Islam, S. Asha, and M. Alathbah, "Design of a modified MIMO antenna based on tweaked spherical fractal geometry for 5G new radio (NR) band N258 (24.25–27.25 GHz) applications," *Fractal and Fractional*, vol. 7, no. 10, Sep. 2023, doi: 10.3390/fractalfract7100718.

BIOGRAPHIES OF AUTHORS

Nidal Qasem    received his B.Sc. degree in electronics and communications engineering (Honours) from Al-Ahliyya Amman University, Amman, Jordan, in 2004. He obtained his M.Sc. degree in digital communication systems for networks and mobile applications (DSC) in 2006, followed by a Ph.D. in wireless and digital communication systems, both from Loughborough University, Loughborough, United Kingdom. He currently holds the position of full professor in the Department of Communications and Computer Engineering at Al-Ahliyya Amman University. His research interests include propagation control in buildings, specifically improving the received power, FSS measurements and designs, antennas, ultra-wide band, orbital angular momentum, and wireless system performance analyses. He is a senior member of the IEEE. He can be contacted at email: Ne.qasem@ammanu.edu.jo.



Mohammad Alkhawatrah    received the B.S. and M.S. degrees in communication engineering from Al-Ahliyya Amman University (AAU), Amman, Jordan, in 2008 and 2016, respectively. He received the Ph.D. degree from the Signal Processing and Networks Research Group in 2020 from Wolfson School of Mechanical, Electrical and Manufacturing Engineering at Loughborough University, Loughborough, U.K. He is currently an assistance professor in electronic and communication department in Al-Ahliyya Amman University. His research interests include buffer-aided relays, non-orthogonal multiple access, relay selection, machine learning, AI, cooperative networks and signal processing. He can be contacted at email: M.alkhawatrah@ammanu.edu.jo.